Impacts of AMSU-A/MHS and IASI Data Assimilation on Temperature and Humidity Forecasts with GSI/WRF over the Western United States

YANSONG BAO[1,2], JIANJUN XU[2]*, ALFRED M. POWELL, JR[4] , MIN SHAO[2,3]

[1] Collaborative Innovation Center on Forecast and Evaluation of Meteorological Disasters, Key Laboratory for Aerosol-Cloud-Precipitation of China Meteorological Administration, Nanjing University of Information Science and Technology, Nanjing, China
[2] Global Environment and Natural Resources Institute, College of Science, George Mason University, Fairfax, Virginia, USA
[3] School of Atmospheric Science, Nanjing University, Nanjing, China
[4] Center for Satellite Applications and Research (STAR), National Oceanic and Atmospheric Administration (NOAA), College Park, Maryland

August 06, 2015

Revised

Atmospheric Measurement Techniques

**Corresponding author contact information:*
Dr. JIANJUN XU, Global Environment and Natural Resources Institute (GENRI) , College of Science, George Mason University. Email: jxu14@gmu.edu

Abstract

Using NOAA's Gridpoint Statistical Interpolation **(**GSI) data assimilation system and NCAR's Advanced Research WRF (ARW-WRF) regional model, six experiments are designed by (1) control experiment (CTRL) and five data assimilation (DA) experiments with different data sets including (2) conventional data only (CON), (3) microwave data (AMSU-A + MHS) only (MW), (4) infrared data (IASI) only (IR), (5) a combination of microwave and infrared data (MWIR), and (6) a combination of conventional, microwave and infrared observation data (ALL). One month experiments in July 2012 and the impacts of data assimilation on temperature and moisture forecasts at the surface and four vertical layers, over the western United States have been investigated. The four layers include lower troposphere (LT) from 800 to 1000 hPa, middle troposphere (MT) from 400 to 800 hPa, upper troposphere (UT) from 200 to 400 hPa and lower stratosphere (LS) from 50 to 200 hPa. The results show that the regional GSI/WRF system is underestimating the observed temperature in the LT and overestimating in the UT and LS. The MW DA reduced the forecast bias from the MT to the LS within 30-hour forecasts, and the CON DA kept a smaller forecast bias in the LT for 2-day forecasts. The largest RMS error is observed in the LT and at the surface (SFC). Compared to the CTRL, the MW DA made the most positive contribution in the UT and LS, and the CON DA mainly improved the temperature forecasts at the SFC. However, the IR DA made a negative contribution in the LT.

Most of the observed humidity in the different vertical layers is overestimated in the humidity forecasts except in the UT. The smallest bias in the humidity forecast occurred at the SFC and UT. The DA experiments apparently reduced the bias from the LT to UT, especially for the IR DA experiment, but the RMS errors are not reduced in the humidity forecasts. Compared to the CTRL, the IR DA experiment has a larger RMS error in the moisture forecast although the

smallest bias is found in the LT and MT.

Key words: Data assimilation, temperature, humidity, forecast

1. Introduction

Instead of the random distribution and heterogeneous spatial density in the traditional conventional radiosondes, satellite observations provide a large amount of data covering worldwide areas for improving the initialization of the weather forecasts models through a data assimilation system. Many studies demonstrated that the assimilation of satellite data significantly improved weather forecasts (Eyre 1992; Andersson et al. 1991; Derber and Wu 1998; Zhou et al. 2011), especially over some areas with sparse conventional observations (McNally et al. 2000; Zapotocny et al. 2008; Liu et al., 2012)

The Meteorological Operational satellite program (MetOp) launched its first polar orbiting satellite (MetOp-A) on October 19, 2006. MetOp-A is in a sun-synchronous orbit, carrying a payload of 10 scientific instruments including the Advanced Microwave Sounding Unit-A (AMSU-A), Microwave Humidity Sounder (MHS) and the new generation Infrared Atmospheric Sounding Interferometer (IASI) to make atmospheric soundings at various altitudes. IASI (Collard 2007; Clerbaux, et al. 2009) measures the radiance emitted from the Earth in 8461 channels covering the spectral interval 645-2760 cm^{-1} at a resolution of 0.5 cm^{-1} (apodized) and with a spatial sampling of 18 km at nadir. Limited spectral data is currently transmitted, stored and assimilated. Rabier et al. (2002) compared a number of techniques for channel selection from high-spectral-resolution infrared sounders, and concluded that the channel-selection method of Rodgers (1996, 2000) is the optimal method.

This study focuses on assessing the effects of AMSU-A, MHS and IASI data assimilation on numerical weather forecasts over the western United States. The model, data and methodology are presented in the section 2 and section 3, respectively. Section 4 describes the results of experiments. The results are summarized and discussed in section 5.

2. Model

2.1 The GSI system for ARW-WRF Regional Model

The assimilation system used here is the Gridpoint Statistical Interpolation (GSI) analysis system, which is developed by United States National Centers for Environmental Prediction (NCEP). The current GSI regional analysis system accepts NCEP's Nonhydrostatic Mesoscale Model (NMM) WRF and NCAR's Advanced Research WRF (ARW) WRF mass core (Liu and Weng, 2006; Xu and Powell, 2011; Wan and Xu, 2011). The interfaces are specialized separately for the WRF NMM core and the WRF ARW core. The analysis system produces an analysis through the minimization of an objective function given by

$$J = \frac{1}{2}(x - x^b)^T B^{-1}(x - x^b) + \frac{1}{2}(H(x) - y^o)^T R^{-1}(H(x) - y^o)$$

where x is the analysis state, B is the background error covariance matrix, x^b is the first guess that comes from GFS 6-h forecast field in this study, H is the transformation operator from the analysis variable to the form of the observations, y^o is the observation such as AMSU-A, MHS, IASI, etc.

The minimization algorithm is composed of two outer iterations to account for weak nonlinearities in the cost function. In the first external iteration the first guess is a 6-h forecast, while in the second one it is the solution from the previous outer iteration. In the cost function based on the NMC method (Parrish and Derber, 1992), B has been estimated from scaled differences between 24-h and 48-h forecasts valid at the same time. The observation error covariance matrix (R) contains information on the observational error and errors in representativeness, which has been calculated before running the GSI.

2.2 Radiative Transfer Model

The radiative transfer model incorporated into the GSI data assimilation system at the NCEP is the Community Radiative Transfer Model (CRTM). The CRTM was developed by the United States Joint Center for Satellite Data Assimilation (JCSDA) for rapid calculations of satellite radiances based on radiative transfer (RT) theory (Han, et al. 2006). The forward model, tangent-linear, adjoint and K-matrix models were also developed for the data assimilation of satellite data: CRTM is always updated for new satellite data. It supports a large number of sensors onboard geostationary and polar-orbiting satellites, covering the microwave, infrared and visible frequency regions.

The CRTM comprises four major modules: (1) RT solution module, (2) atmospheric transmittance module, (3) surface emissivity/reflectivity module, (4) particle scattering module. Six RT solution schemes were tested in the CRTM (Weng et al., 2007). According to several performance factors, the advance doubling and adding scheme (ADA; Liu and Weng, 2006) was selected for the CRTM implementation. In CRTM, a fast and optimal spectral sampling (OSS) absorption model (Moncet et al. 2004) is used to calculate atmospheric transmittance.

2.3 Experiment Design

The objective of this study is to explore the effect of satellite data assimilation on the main atmospheric state forecast by comparing the results from microwave (AMSU-A and MHS), hyperspectral infrared radiance (IASI) and conventional data assimilation. Over the main continent of United States of America (USA), there are many conventional observation stations which can be used to validate the forecast results. Therefore, the western coast region of the USA is selected as the experimental region. There were more satellite data coverage of the experimental region around 18 UTC than other time, such as 00, 06, 12 and 18 UTC. The covered region at 18 UTC is 20º - 55ºN and 85º - 155ºW, which includes the western USA and

sea area near the west coast (Figure 1).

The experiment design includes six simulations (Table 1). The control (CTRL) experiment is first made with an initial time at 18:00 UTC from 30 June to 30 July and makes 6-h forecasts. The five data assimilation (DA) experiments and the continued control experiment are made with initial time at 00:00 UTC from July 1 to 31, 2012 and make a 72-h forecast for each day. The initial condition in all six experiments is obtained from the 6-h forecasts of the first control experiment. The five DA experiments are made with different data sets including conventional data (CON), microwave data (AMSU-A + MHS) (MW), infrared data (IASI) (IR), a combination of microwave and infrared data (MWIR), a combination of conventional, microwave and infrared observation data (ALL). The initial conditions and lateral boundary conditions came from the operational GFS forecast at 6-h intervals and 0.5 x 0.5 degree resolution, which were downloaded from NCEP data inventory (ftp://ftp.ncep.noaa.gov/pub/data/ nccf/com/gfs/prod/).

In the ARW model, the physics of the model includes the Goddard Cumulus Ensemble (GCE) microphysics scheme, Yonsei University planetary boundary layer (PBL) scheme, Noah land surface model, Rapid Radiative Transfer Model (RRTM) longwave radiation, and the Goddard shortwave radiation scheme (Xu et al., 2009). The 15-km WRF model forecast with a mesh size domain of 718 X 373 (Fig.1) was used. Forty-three (43) vertical layers were selected for use with a model top of 10 hPa.

3. Data and Methodology

3.1 Conventional and Satellite data

In this study, the conventional observation data includes atmospheric temperature (T), moisture (Q) and wind speed (WSP) at various pressure levels and pressure data at the surface that were downloaded from NCEP data inventory (ftp://ftp.ncep.noaa.gov/pub/data/

nccf/com/gfs/prod/). Figure 1a shows the distribution of the conventional data on July 1, 2012 where the atmospheric temperature, moisture and surface pressure observations are rare. Most of atmospheric temperature and moisture observations are conducted at the surface level in the pressure range of 1000-1200 hPa. Most of the WSP data are found over the sea close to the western coast of the United States.

The satellite data includes the Advanced Microwave Sounding Unit-A (AMSU-A), Microwave Humidity Sounder (MHS) and the new generation Infrared Atmospheric Sounding Interferometer (IASI). Figure 1b shows the distribution of the AMSU-A, MHS and IASI datasets acquired about at 18:00 UTC on July 1, 2012. AMSU-A is a 15-channel cross-track, stepped-line scanning, total power microwave radiometer. In this study the channels from 4 to 14 are assimilated, which were designed to detect atmospheric temperature at 11 layers from the surface to around 45 km. Their weighting function is illustrated in Figure 2a. MHS on the other hand probes at millimetric frequencies between 89 and 183 GHz, the channels from 2 to 5 are assimilated, which were designed to detect atmospheric moisture at 2 layers from surface to around 400 hPa. Their weighting function is illustrated in Figure 2b. Channel 4 of AMSU-A and channel 2 of MHS can detect the atmospheric temperature and humidity at the lowest layer of the troposphere. Channels 5 and 6 of AMSU-A and channels 3, 4 and 5 of MHS can represent the atmospheric temperature and humidity in the middle atmospheric layer of the troposphere. Channel 7 of AMSU-A can indicate the atmospheric temperature in the highest layer of troposphere. Channels 9 and 10 of AMSU-A can detect the atmospheric temperature in lower layer of the stratosphere

The IASI instrument covers the spectral range from the thermal infrared at 3.62 μm (2760 cm^{-1}) to 15.5 μm (645 cm^{-1}) covering the peak of the thermal infrared and particularly the CO2

band with the humidity (Q) branch around 666 cm^{-1}. Within these bands, the selected 279 bands (Table 2) correspond to atmospheric temperature and humidity. A band number smaller than 515 represents atmospheric temperature and a band number larger than 2701 represents atmospheric humidity. Their weighting function is illustrated in Figure 2c.

3.2 Radiance data quality control and bias correction

The radiance data have been preprocessed by NOAA's Satellite and Information Service (NESDIS) before becoming available for usage. The data have been statistically limb corrected (adjusted to nadir) and surface emissivity corrected in the microwave channels and cloud cleared in the tropospheric channels. Although the satellite data have undergone preprocessing, they need further bias correction before being ingested into data assimilation system. The source of the biases can be related to instrument calibration problems, and predictor and zenith angle bias. It was demonstrated that a successful bias correction scheme must take into account the spatially varying and air-mass dependent nature of radiance biases (Kelly and Flobert, 1988; McMillin et *al.*, 1989; Uddstrom, 1991). Eyre (1992) and Harris and Kelly (2001) categorized the bias into two types: scan bias and air-mass bias, and presented a bias correction scheme. GSI uses this bias correction scheme to correct radiance bias. The radiance bias correction coefficients maybe downloaded from Global Data Assimilation System (GDAS) data directory(ftp://ftp.ncep.noaa.gov/pub/data/ nccf/com/gfs/prod/), and it can be used to correct the radiance bias in GSI. To that purpose, monthly regional meaninnovations, e.g. observation minus background (OMB) and observation minus analysis (OMA), are calculated with or without bias corrections in this study. For example, Fig. 3 shows the scattering plots of surface pressure (Fig. 3a), atmospheric temperature at the height of 2m (Fig. 3b) and wind speed at the height of 10m (Fig. 3c) between OMB and OMA in the ALL data experiment. The result shows

that the slope of the simulated line is less than 1, which indicates the analysis fields are closer to observation than background fields.

3.3 Methodology

In order to evaluate the effects of radiance data assimilation on temperature and moisture at the different vertical layers, the surface (SFC) and four atmospheric layers are examined. The four layers include lower troposphere (LT) from 800 to 1000 hPa, middle troposphere (MT) from 400 to 800 hPa, upper troposphere (UT) from 200 to 400 hPa and lower stratosphere (LS) from 50 to 200 hPa. Similar to a previous study (Xu, et al., 2009), two statistical variables - bias and root mean square (RMS) errors are investigated.

If X represents any of the parameters under consideration for a given time and vertical level, then the forecast error is defined as $X' = X_f - X_o$ where the subscripts *f* and *o* denote forecast and observed quantities, respectively. Given N valid pairs of forecasts and observations, the bias is computed as

$$bias = \overline{X'} = \frac{1}{N}\sum_{i=1}^{N} X_i' \qquad (1)$$

the root mean-square (RMS) error is computed as

$$RMS = \sqrt{\frac{1}{N}\sum_{i=1}^{N}(X_i')^2} \qquad (2)$$

The bias and RMS error at 00:00 and 12:00 UTC are calculated because more than enough observational data and approximately 3000 sounding stations can be used at the two times.

4. Results

4.1 Impact of DA on temperature

At the SFC, the CON (conventional data only) DA experiment shows (Fig.4a) the smallest bias value in all six experiments. The three involving infrared satellite DA experiments (IR,

IR+MW, IR+MW+CON) show a larger bias than the CTRL experiment. For the first 24 hours, it seems that satellite radiance DA, especially for the infrared IASI data, make a negative contribution to the temperature forecasts. In addition, the bias characterized a diurnal cycle feature for the 72-h forecasts, with the smaller bias appearing at 06, 30, 54 and 72-h corresponding to a local time at 4:00 pm while the higher bias appeared at 18, 42 and 66-h corresponding to 4:00 am local time.

Compared to the SFC, the LT shows a more clear diurnal variation (Fig. 4b), and all model forecasts underestimated the observed temperature. The CTRL and CON experiments obtained the smallest forecast bias.

Different from the SFC and LT, the diurnal variation of bias disappeared in the MT (Fig. 4c). Compared to the CTRL experiment, the bias is significantly reduced in all DA experiments especially for the two combination experiment (MWRI and ALL), the bias is almost zero within the 30-h forecast. It implies that both MW (AMUS-A and MHS) and IR (IASI) DA give a positive contribution to the accuracy of temperature forecasts at the MT.

At the UT, the smaller bias appeared in the CON and MW DA experiments (Fig. 4d), and the combination DA experiments (MWIR and ALL) show a larger bias than the CTRL experiment. The results indicate that the IR DA gave a negative contribution to the temperature forecasts and the MW experiment improved the forecast accuracy in the UT.

In contrast, the bias in the LS indicates an opposite pattern to the SFC and LT where all satellite DA experiments reduced the forecast bias (Fig. 4e). The result demonstrated that the conventional DA did not improve the forecasts because of the sparse observational data used in this layer. The MW DA obtained the smallest bias in the LS.

In order to clearly understand the different performance in the six experiments, the

temperature forecast bias profile at 6-h, 30-h and 54-h has been examined. Fig. 5 indicates a similar pattern at the three forecast times where the lower bias can be found at the SFC and MT while the larger bias appeared at the UT and LS. Generally, the model forecasts overestimated the observed temperature except in the LT. Compared to the CTRL experiment, the four satellite DA experiments (MW, IR, MWIR and ALL) show a smaller bias from the MT through LS, but the forecasts did not get improved in the LT below 800 hPa. In contrast, the CON experiment has better performance in the LT, especially at the SFC.

It is obvious that the larger bias in temperature forecast appeared in the LT, UT and LS, but the model is underestimating the observed temperature in the LT and overestimating in the UT and LS (Fig. 5). The satellite DA, especially for the MW DA experiment using AMSU-A, reduced the forecast bias at the levels from the MT to LS. Meanwhile, the CON DA has a smaller forecast bias in the LT, especially at the SFC. Note the IR experiment using the IASI data produced a worst result in the LT.

The forecast RMS error demonstrated some different features (Fig. 6). First, the RMS error reduced the diurnal variation and it significantly increased with the extended length of forecast time at the SFC. The RMS error in the CON and MW experiments is slightly less than that in the CTRL experiment and the other three satellite DA experiments within 24-h forecasts (Fig. 6a). Second, consistent with the larger negative bias in all the satellite DA experiments (Fig. 4b) in the LT, larger RMS errors are observed in these DA experiments (Fig. 6b) compared to the CRTL. Third, different from the smaller bias in the DA experiments, the larger RMS errors are maintained in the DA experiments in the MT (Fig. 6c). Fourth, the CON and MW experiments improved the temperature forecasts in the UT (Fig. 6d). But in the LS, the microwave DA experiments including MW, MWIR and ALL indicate smaller RMS errors than the CTRL

experiments (Fig. 6e). It is apparent that the CON DA gave a negative contribution to the temperature forecast in the LS.

Corresponding to the bias profile (Fig. 5), the forecast RMS error profile at 6-h, 30-h and 54-h indicates (Fig. 7) that the smallest RMS error is observed at the MT and the largest RMS error appeared in the LT and SFC. Compared to the CTRL experiment, the smaller RMS errors are only found in the MW experiment in the UT and LS, and the CON DA made a positive contribution at the SFC and UT.

The results clearly show the IR DA experiment gives a negative contribution to the temperature forecast in the regional system. But the MW DA experiment shows a positive impact at the LS, and the CON experiment displays better performance at the SFC and UT. It is worth noticing that the RMS error is not always consistent with the bias in the temperature forecasts, for example, the smaller bias appeared at the SFC while a larger RMS error is observed there.

4.2 Impact of DA on humidity

Similar to the temperature forecasts at the SFC, the diurnal variation of the moisture bias is observed and the smallest bias appeared in the CON and CTRL experiments within the 42-h forecast (Fig. 8a) with largest bias occurring in the MWIR experiment at 18-h. It is clear that all four satellite DA experiments do not improve the moisture forecast compared to the CTRL experiment. In contrast, the IR DA produced a larger bias significantly different from the other experiments in the entire troposphere (Fig. 8b,c,d). It seems to tell us that the IR DA significantly impacts the humidity forecasts in the troposphere. However, the impacts disappeared in the LS (Fig. 8e).

Compared to the bias profile of the temperature forecast (Fig 4), all model runs

overestimated the observed humidity except for the UT. The smallest bias in the humidity forecast occurred at the SFC and UT (Fig. 9). Most of DA experiments apparently reduced the bias from LT to UT, especially for the IR experiment. But it is worth noting that the MW DA has a larger bias than the CTRL experiment in the whole troposphere.

However, the RMS error in the humidity forecasts (Fig. 10) increases from the SFC to LS. The largest error in the UT and LS is almost double the amount at the SFC. In addition, most of DA experiments demonstrated a larger RMS error than that in the CTRL experiment. In other words, the DA experiments gave a negative contribution to the humidity forecasts. The IR DA experiment did not improve moisture forecast although its bias is very small at the LT and MT.

5. Summary and Discussion

5.1 Summary

In this study, six experiments were designed to assess the effects of data assimilation on atmospheric temperature and moisture forecasts over the western United States. The results are summarized as follows.

The regional model underestimates the observed temperature in the LT and overestimates it in the UT and LS. The MW experiment reduced the forecast bias from the MT to LS, and the CON DA obtained a smaller forecast bias in the LT, especially at the SFC. But the IR experiment using the IASI data obtained the largest bias in the LT.

However, the RMS error is not always consistent with the bias profile in the temperature forecasts: in fact, the RMS error profile shows that the largest RMS error appeared in the LT and the smallest error in the MT. Compared to the CTRL experiment, the smaller RMS errors are only found in the MW experiment in the UT and LS, and the CON DA gave a positive contribution at the SFC and in the UT. The IASI DA experiment has a negative impact on the

temperature forecast in the regional forecast system.

In contrast, all model forecasts overestimated the observed humidity except in the UT. The smallest bias in the humidity forecast occurred at the SFC and in the UT. Most of DA experiments apparently reduced the bias in the LT to UT, especially for the IR DA experiment. But the MW DA obtained a larger bias than the CTRL experiment in the entire troposphere.

The RMS error in the humidity forecasts increases from the SFC to the LS, which is similar to the bias profile except in the UT. The largest error in the UT and LS is almost double the amount at the SFC. The DA experiments give a limited contribution to the humidity forecasts. The IR DA experiment does not improve the moisture forecast although its smallest bias is found in the LT and MT.

5.2 Discussion

In this is study, the WRF-ARW mesoscale model was linked to GSI data assimilation system, the impacts of AMSU-A/MHS and IASI radiance data assimilation on the temperature and humidity forecasts have been investigated. Due to the complexity of measurements for satellite instruments (such as IASI has 8461 channels) and lack of knowledge in the estimation of impacts of those datasets in this regional area, forecasters should be aware of the limitations of these data assimilation.

The results show that the bias and forecast error is substantially related to the vertical layer of the objective. For example, the AMSU-A data assimilation reduced the temperature forecast bias in the upper atmospheric layers, the conventional data assimilation indicates the best performance in the lower layer, but the IASI data assimilation shows worst performance in the lower layer. Compared to the largest bias in the upper atmospheric layer, the largest RMS error appeared in the lower atmospheric layers. For the humidity forecast there is a different

behavior: the IASI data assimilation significantly reduced the bias in the troposphere, but the RMS error tells us that the IASI data assimilation does not improve the moisture forecast in this layer. The reason is very complicated, it is partially attributed to the data selection processes of the data assimilation. The results showed in this analysis demonstrate the partial impact of satellite data on temperature and humidity forecasts in this region, but the positive or negative impact depends on the atmospheric layer and forecasts variables.

It is worth noting that the results presented here are based on one month's forecasts with three satellite instruments. The model performance needs to be examined with longer experiments and more data selection that extend to all available satellite data sets and more experiments from the different areas. As expressed by Manning and Davis (1997), "These statistics would provide additional information to model users and alert model developers to those research areas that need more attention."

Acknowledgements.

The GSI data assimilation system was obtained from Joint Center for Satellite Data Assimilation (JCSDA), WRF-ARW model was obtained from the NCAR, the satellite datasets were provided by NOAA/NESDIS/STAR. The authors would like to thank these agencies for the model and data providing. This work was partially supported by a project funded by the Priority Academic Program Development of Jiangsu Higher Education Institutions (PAPD), the Major State Basic Research Development Program of China (973 Program: No. 2013CB 430101), the National Natural Science Foundation of China (No. 40701130), the No-for-Profit Industry (Meteorology) Research Program, China (GYHY201106027), and Jiangsu Key Laboratory of Meteorological Observation and Information Processing (S5311026001) at the Nanjing University of Information Science and Technology, Nanjing, China.

This work was partially supported by the National Oceanic and Atmospheric Administration (NOAA), National Environmental Satellite, Data, and Information Service (NESDIS), Center for Satellite Applications and Research (STAR). The views, opinions, and findings contained in this publication are those of the authors and should not be considered an official NOAA or U.S. Government position, policy, or decision.

Reference

Andersson, E., A. Hollingsworth, G. Kelly, P. Lönnberg, J. Pailleux, and Z. Zhang, 1991: Global observing system experiments on operational statistical retrievals of satellite sounding data. *Mon. Wea. Rev.,* **119,** 1851–1864.

Clerbaux C,. A. Boynard , L. Clarisse , M. George , J. Hadji-Lazaro , H. Herbin , D. Hurtmans , M. Pommier, A. Razavi , S. Turquety, C. Wespes and P.-F. Coheur, 2009: Monitoring of atmospheric composition using the thermal infrared IASI/MetOp sounder. Atmos. Chem. Phys., 9, 6041– 6054, 2009. www.atmos-chem-phys.net/9/6041/2009/

Collard AD. 2007. Selection of IASI channels for use in numerical weather prediction. *Q. J. R. Meteorol. Soc.* **133**: 1977–1991

Derber J. C. and W-S Wu. 1998: The use of TOVS cloud-cleared radiances in the NCEP SSI analysis system. *Mon. Wea. Rev.*, **126**, 2287–2299.

Eyre J. A bias correction scheme for simulated TOVS brightness temperatures. Tech. Memo. 186, ECMWF (1992).

Han Y., Paul van Delst, Q. Liu, F. Weng, B. Yan, R. Treadon and J. Derber, 2006: JCSDA Community Radiative Transfer Model (CRTM) - Version 1, *NOAA Tech Report 122*.

Harris B. and Kelly G., A satellite radiance bias correction scheme for data assimilation Quart. J. Roy. Meteorol. Soc. 127, 1453 (2001).

Kelly GA, Flobert JF. 1988. Radiance tuning. In: TechnicalProceedings of the Fourth International TOVS Study Conference, Igls, Austria, 16–22 March 1988: 99–117.

Liu Q, Weng F. Detecting the warm core of a hurricane from the Special Sensor Microwave Imager Sounder. *Geophys. Res. Lett.* 2006; 33: L06817, doi:10.1029/2005GL025246.

Liu, Q., and F. Weng, 2006: Advanced doubling–adding method for radiative transfer in planetary atmosphere. *J. Atmos. Sci.*, **63,** 3459–3465.

Liu, Zhiquan, Craig S. Schwartz, Chris Snyder, and So-Young Ha. "Impact of assimilating AMSU-A radiances on forecasts of 2008 Atlantic tropical cyclones initialized with a limited-area ensemble Kalman filter", Monthly Weather Review, 2012.

Manning, K. W., and C. A. Davis, 1997: Verification and sensitivity experiments for the WISP95 MM5 forecasts. *Weather Forecasting*, **12**, 719–735

McMillin, L. M., L. J. Crone, and D. S. Crosby, 1989: Adjusting satellite radiances by regression with an orthogonal transformation to a prior estimate. J. Appl.Meteor., 28, 969–975.

McNally, A. P., J. C. Derber, W. Wu, and B. B. Katz, 2000: The use of TOVS level-1b radiances in the NCEP SSI analysis system. *Quart. J. Roy. Meteor. Soc.*, **126**, 689–724.

Moncet, J., G. Uymin, and H. E. Snell, 2004: Atmospheric radiance modeling using the Optimal Spectral Sampling (OSS) method. Preprints, *SPIE Defense and Security Symp., Conf. 5425: Algorithms and Technologies for Multispectral, Hyperspectral, and Ultraspectral Imagery X*, Orlando, FL, Society of Photo-Optical Instrumentation Engineers, 5425–5437.

Nutter, P. A., and J. Manobianco, 1999: Evaluation of the 29-km Eta Model. Part I: Objective verification at three selected stations. Wea. Forecasting, 14, 5–17.

Parrish DF, Derber JC (1992) The National Meteorological Center’s spectral statistical

interpolation analysis system. Mon Wea Rev 20:1747–1763

Rabier F, Fourri´e N, Chafa¨ı D, Prunet P. 2002. Channel selection methods for Infrared Atmospheric Sounding Interferometer radiances. *Q. J. R. Meteorol. Soc.* **128**: 1011–1027.

Rodgers CD. 1996. 'Information content and optimisation of high spectral resolution measurements'. pp 136–147 in: *Optical Spectroscopic Techniques and Instrumentation for Atmospheric and Space Research II*, SPIE 2380, Hays PB, Wang J (eds).

Rodgers CD. 2000. *Inverse Methods for Atmospheres: Theory and Practice*. World Scientific: Singapore.

Uddstrom, M., 1991: Forward model errors. Proc. 6th Int. TOVS Study Conference, Airlie, Virginia, Cooperative Institute for Meteorological Satellite Studies, Space Science and Engineering Center, University of Wisconsin, USA, 501–516.

Wan, Q. and J Xu, 2011: A numerical study of the rainstorm characteristics of the June 2005 flash flood with WRF/GSI data assimilation system over south-east China. *Hydrological Processes*, **25**, 1327–1341 (2011) DOI: 10.1002/hyp.7882

Weng F., 2007: Advances in Radiative Transfer Modeling in Support of Satellite Data Assimilation. *J. Atmos. Sci.*, **64**, 3799–3807

Xu J., S. Rugg, L. Byerle, and Z. Liu, 2009: Weather Forecasts by the WRF-ARW Model with the GSI Data Assimilation System in the Complex Terrain Areas of Southwest Asia. *Wea. Forecasting*, **24**, 987–1008.

Xu, J and A Powell, 2011: Dynamical Downscaling Precipitation over the Southwest Asian: Impacts of Radiance Data Assimilation on the Hindcasts of the WRF-ARW Model, *Atmospheric Research***.** doi:10.1016/j.atmosres.2012.03.005

Zapotocny, T. H., Jung, J. A., Le Marshall, J. F. and Treadon, R. E. 2008: A Two Season Impact Study of Four Satellite Data Types and Rawinsonde Data in the NCEP Global Data Assimilation System. Wea. Forecast.,23, 80 – 100.

Zhou, H., G´omez-Herna´ndez, J. J., Hendricks Franssen, H.-J., Li, L., 2011. An approach to handling nongaussianity of parameters and state variables in ensemble kalman filtering. Advances in Water Resources.34 (7), 844–864, DOI: 10.1016/j.advwatres.2011.04.014.

Table 1 The experiment design includes six simulations (EXP1-EXP6)

	Experiment	Description	Initial time
EXP1	CTRL	Control experiment without data assimilation	18:00 UTC
EXP2	CON	Conventional data assimilation	00:00 UTC
EXP3	MW	AMSU-A+MHS data assimilation	00:00 UTC
EXP4	IR	IASI data assimilation	00:00 UTC
EXP5	MWIR (MW+IR)	AMSU-A+MHS+IASI data assimilation	00:00 UTC
EXP6	ALL (CON+MW+IR)	Conventional+AMSU-A+MHS+IASI data assimilation	00:00 UTC

Table2 Listed below are the 279 Channels in IASI corresponding to atmospheric temperature and humidity. The numbers indicate the order in which the channels were chosen in current data assimilation

16	135	226	356	566	1658	2993	3248	3509	5502
38	138	230	360	571	1671	3002	3252	3518	5507
49	141	232	366	573	1786	3008	3256	3527	5509
51	144	236	371	646	1805	3014	3263	3555	5517
55	146	239	373	662	1884	3027	3281	3575	5558
57	148	243	375	668	1991	3029	3303	3577	5988
59	151	246	377	756	2019	3036	3309	3580	5992
61	154	249	379	867	2094	3047	3312	3582	5994
63	157	252	381	906	2119	3049	3322	3586	6003
66	159	254	383	921	2213	3053	3375	3589	
70	161	260	386	1027	2239	3058	3378	3599	
72	163	262	389	1046	2271	3064	3411	3653	
74	167	265	398	1121	2321	3069	3438	3658	
79	170	267	401	1133	2398	3087	3440	3661	
81	173	269	404	1191	2701	3093	3442	4032	
83	176	275	407	1194	2741	3098	3444	5368	
85	180	282	410	1271	2819	3105	3446	5371	
87	185	294	414	1479	2889	3107	3448	5379	
104	187	296	416	1509	2907	3110	3450	5381	
106	193	299	426	1513	2910	3127	3452	5383	
109	199	303	428	1521	2919	3136	3454	5397	
111	205	306	432	1536	2939	3151	3458	5399	
113	207	323	434	1574	2944	3160	3467	5401	
116	210	327	439	1579	2948	3165	3476	5403	
119	212	329	445	1585	2951	3168	3484	5405	
122	214	335	457	1587	2958	3175	3491	5455	
125	217	345	515	1626	2977	3178	3497	5480	
128	219	347	546	1639	2985	3207	3499	5483	
131	222	350	552	1643	2988	3228	3504	5485	
133	224	354	559	1652	2991	3244	3506	5492	

Caption of Figures

Fig. 1 Distribution of observations. (a) conventional data on July 1, 2012 with the atmospheric temperature (yellow), moisture (dark blue) and surface pressure(light blue), wind speed (orange). (b) Scan coverage of AMSU-A (light blue), MHS (dark blue) and IASI (red) radiance at 18:00 UTC on July 1, 2012

Fig. 2 Vertical weighting functions for satellite observations as a function of height. (a) AMSUA , (b) MHS , (c) IASI

Fig. 3 The scattering plot between observation minus background [OMB] and observation minus analysis [OMA] in the all data (Conventional+AMSU-A+MHS+IASI) experiement (a: surface pressure, b: atmospheric temperature at the height of 2 meters, c: wind speed at the height of 10 meters) for 1 July 2012

Fig. 4 Bias of the temperature (T) forecasts at (a) surface (SFC), (b) lower troposphere (LT), (c) middle troposphere (MT), (d) upper troposphere (UT), (e) lower stratosphere (LS). Unit: °C. CTRL , CON , MW, IR, MWIR and ALL are defined in Table 1

Fig. 5 Bias profile of the temperature (T) forecasts at (a) 6-h , (b) 30-h, (c) 54-h forecasts. Unit: °C. Other definitions are the same of Fig. 4.

Fig. 6 RMSE of the temperature (T) forecasts at (a) surface (SFC), (b) lower troposphere (LT), (c) middle troposphere (MT), (d) upper troposphere , (e) lower stratosphere. Unit: °C. Other definitions can be found in Table 1.

Fig. 7 The RMSE profile of the temperature forecasts at (a) 6-h , (b) 30-h, (c) 54-h forecasts.

Unit: °C. Other definitions are the same of Fig. 4.

Fig. 8 The bias of the specific humidity (Q) forecasts at (a) surface (SFC), (b) lower troposphere (LT), (c) middle troposphere (MT), (d) upper troposphere , (e) lower stratosphere. Unit: g/kg. Other definition can be found in Table 1.

Fig. 9 Bias profile of the specific humidity forecasts at (a) 6-h , (b) 30-h, (c) 54-h forecasts. Unit: g/kg. Other definitions are the same of Fig. 4.

Fig. 10 The RMSE profile of the specific humidity forecasts at (a) 6-h , (b) 30-h, (c) 54-h forecasts. Unit: g/kg. Other definitions are the same of Fig. 4.

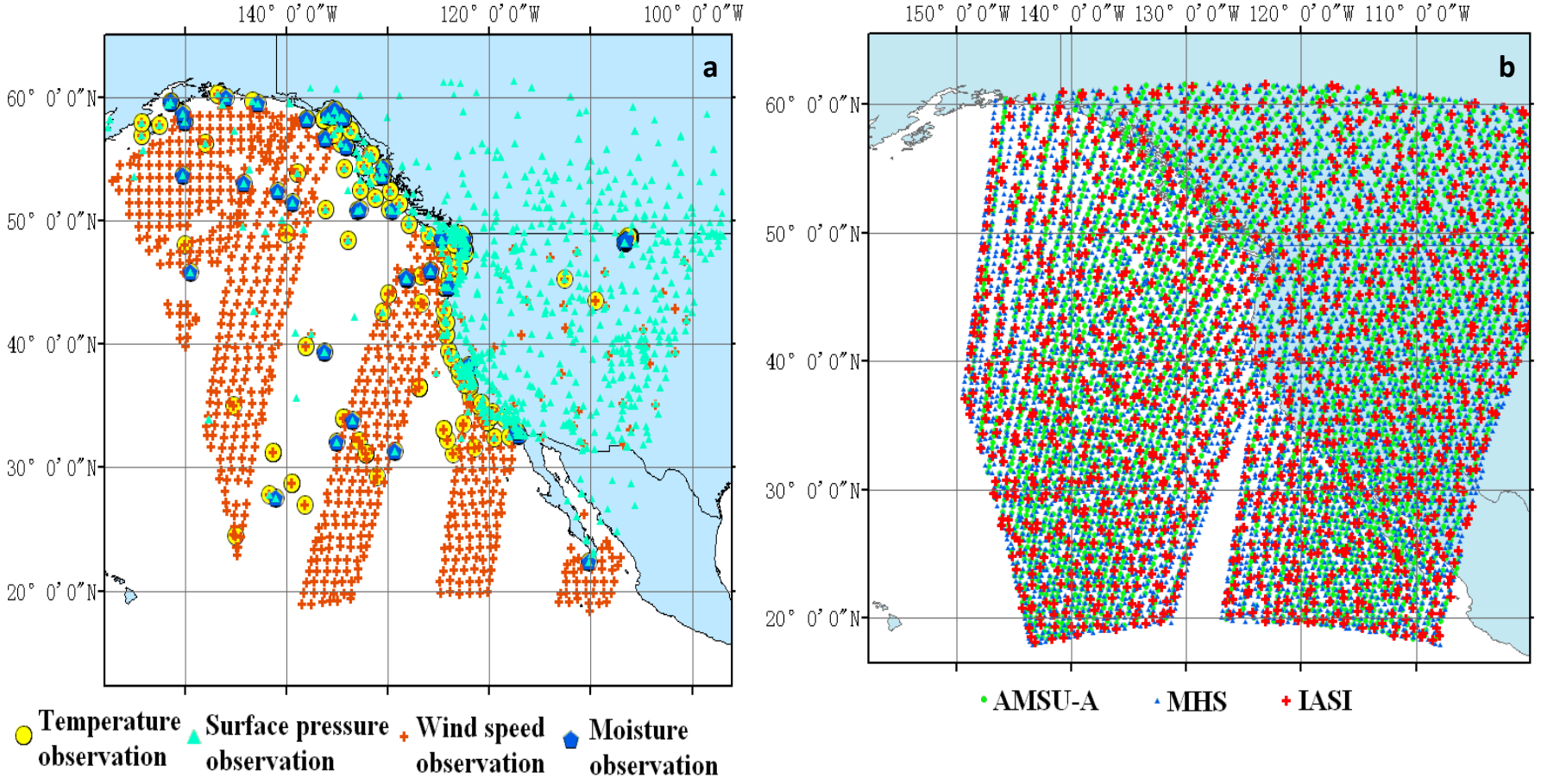

Fig. 1 Distribution of observations. (a) conventional data on July 1, 2012 with the atmospheric temperature (yellow), moisture (dark blue) and surface pressure(light blue), wind speed (orange). (b) Scan coverage of AMSU-A (light blue), MHS (dark blue) and IASI (red) radiance at 18:00 UTC on July 1, 2012

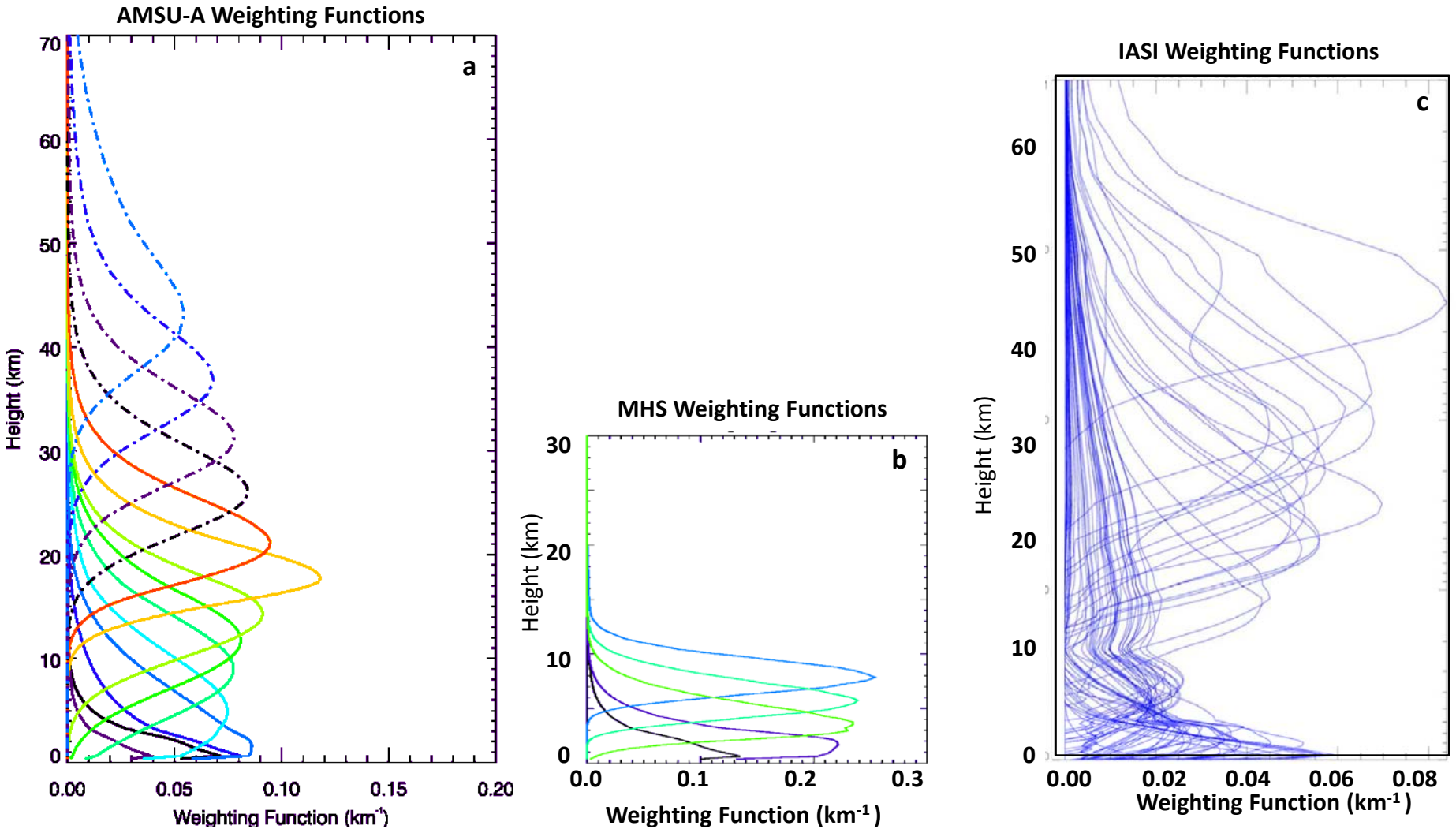

Fig. 2 Vertical weighting functions for satellite observations as a function of height. (a) AMSUA , (b) MHS , (c) IASI

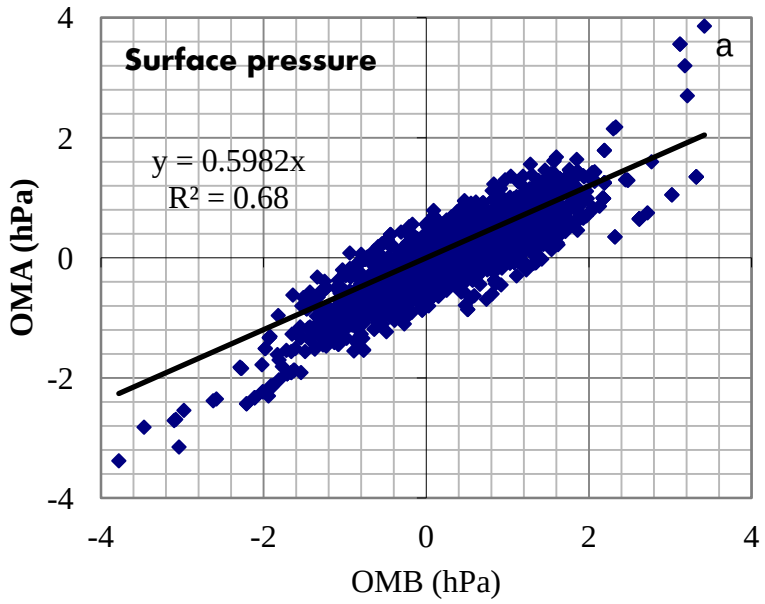

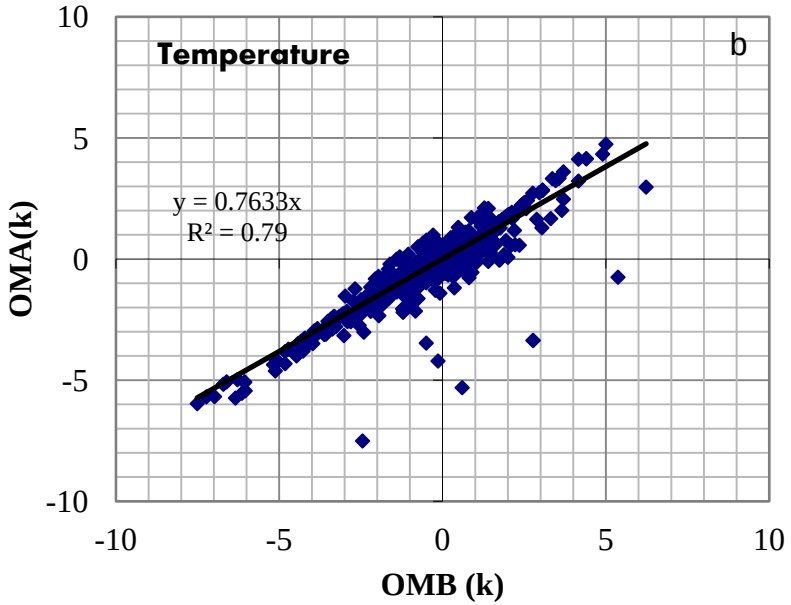

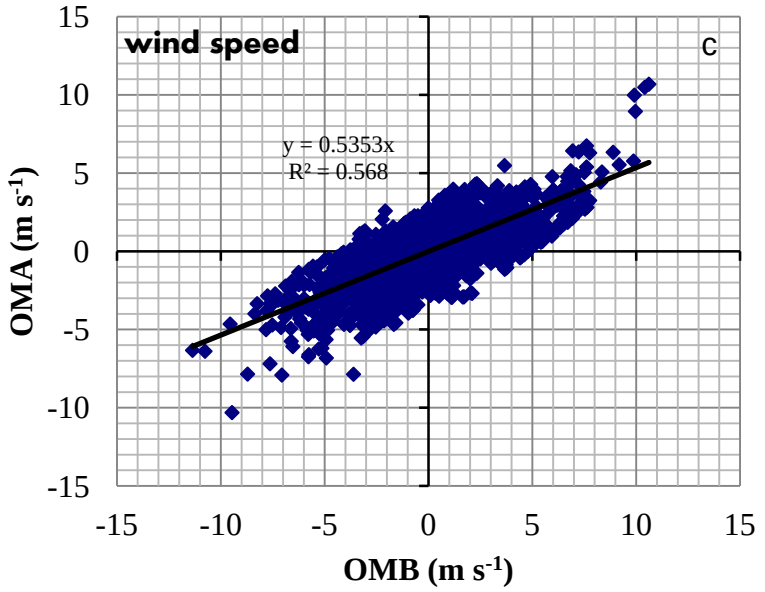

Fig. 3 The scattering plot between observation minus background [OMB] and observation minus analysis [OMA] in the all data (Conventional+AMSU-A+MHS+IASI) experiment (a: surface pressure, b: atmospheric temperature at the height of 2 meters, c: wind speed at the height of 10 meters) for 1 July 2012

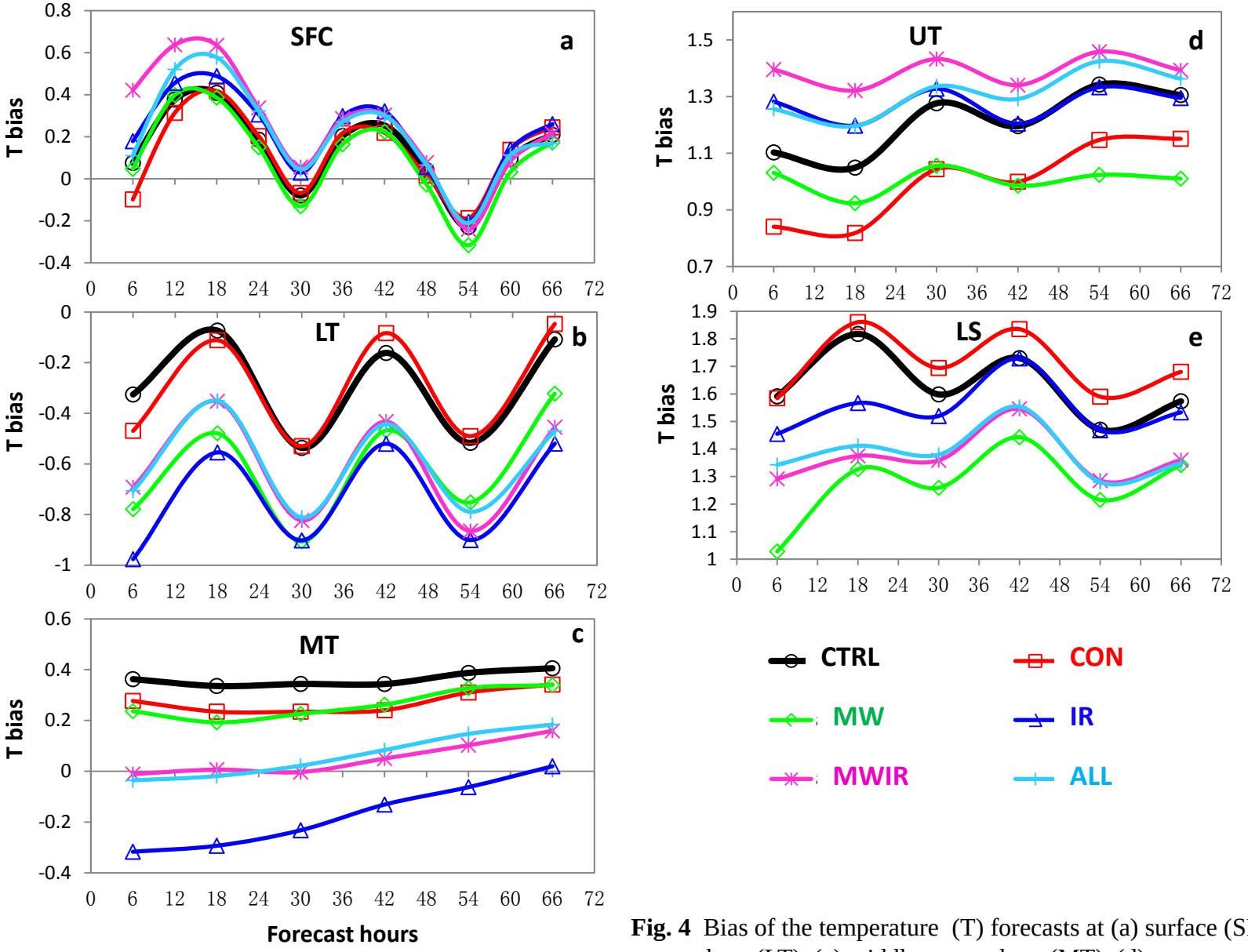

Fig. 4 Bias of the temperature (T) forecasts at (a) surface (SFC), (b) lower troposphere (LT), (c) middle troposphere (MT), (d) upper troposphere (UT), (e) lower stratosphere (LS). Unit: °C. CTRL , CON , MW, IR, MWIR and ALL are defined in Table 1

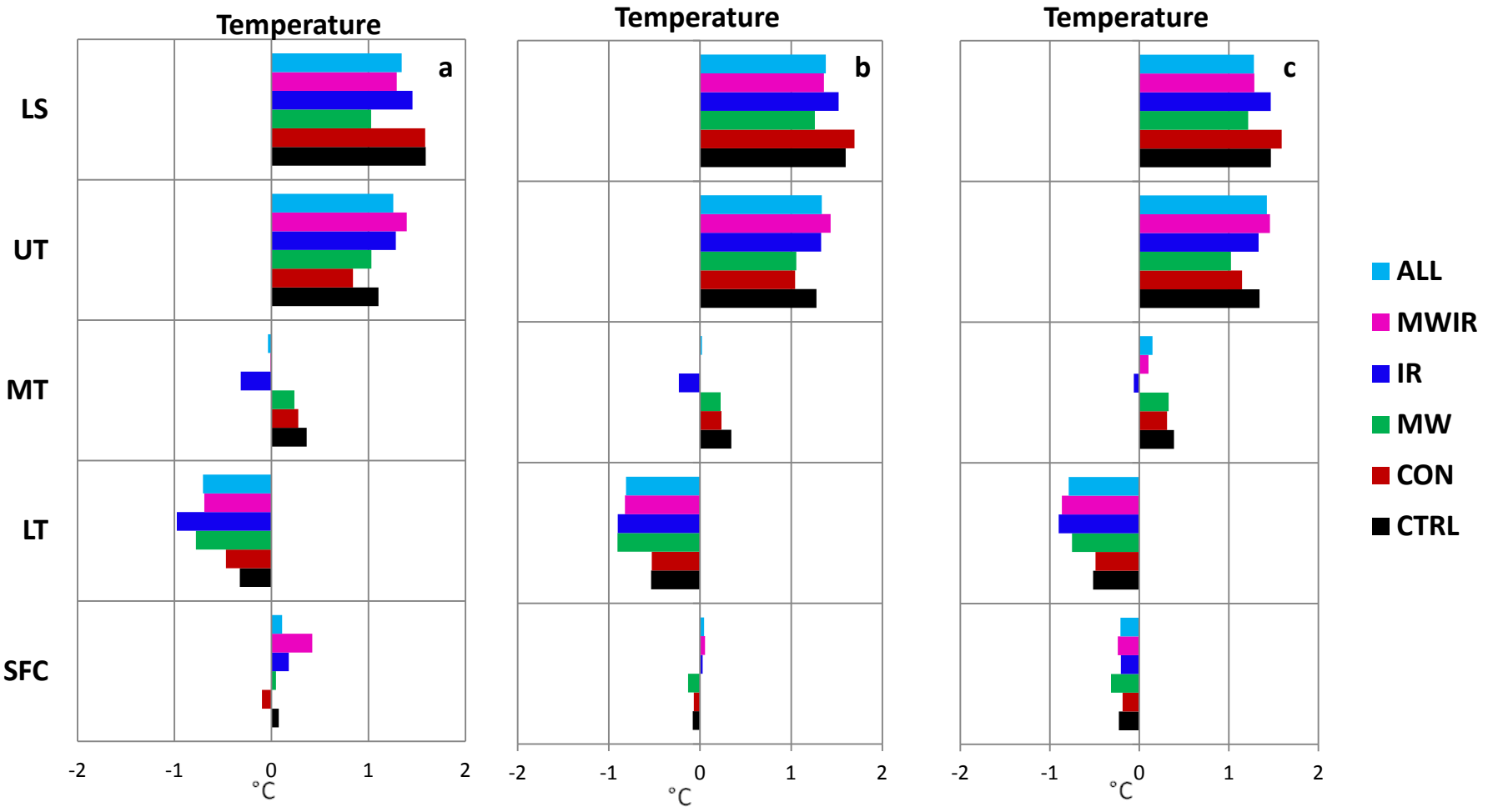

Fig. 5 Bias profile of the temperature (T) forecasts at (a) 6-h , (b) 30-h, (c) 54-h forecasts. Unit: °C. Other definitions are the same of Fig. 4.

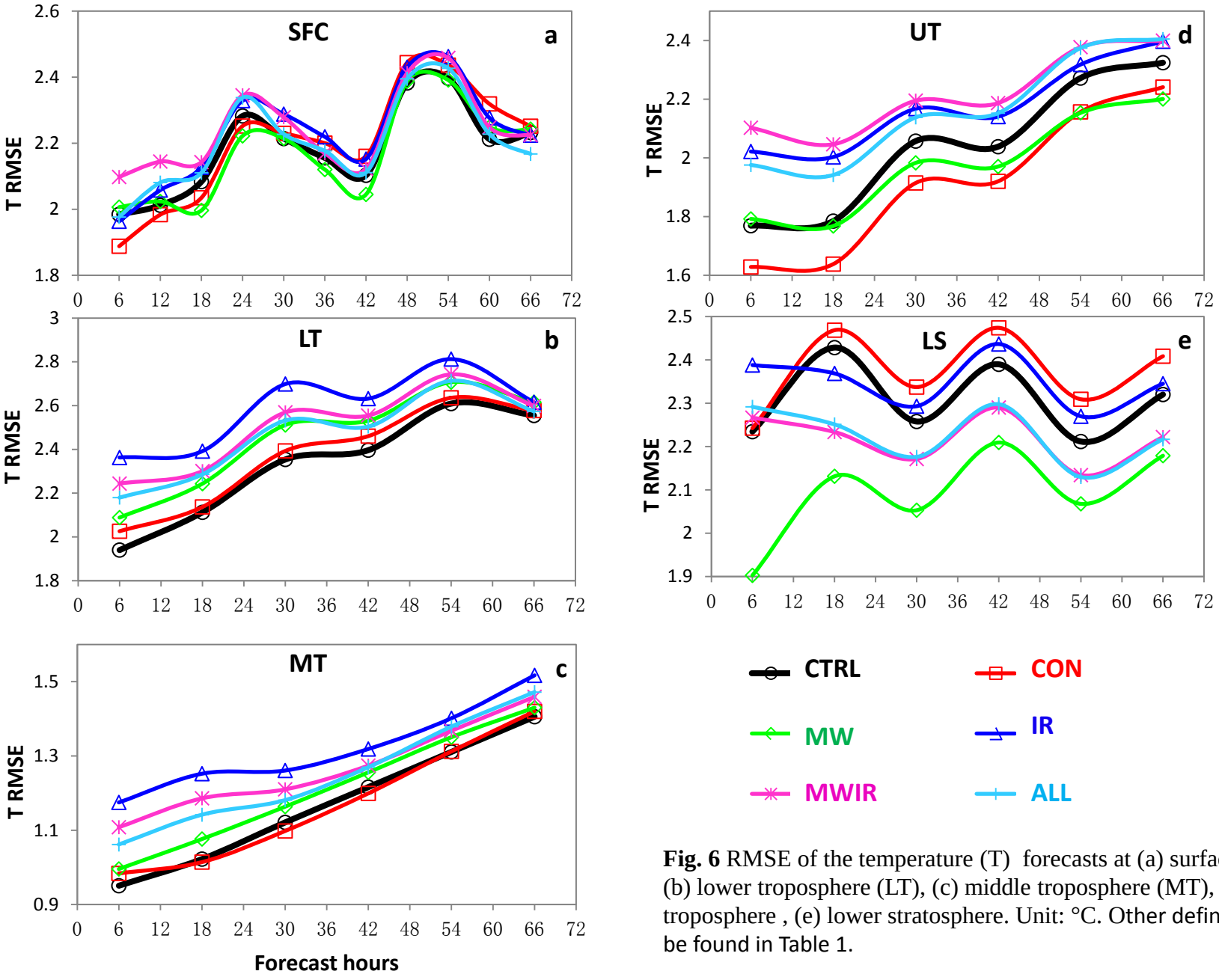

Fig. 6 RMSE of the temperature (T) forecasts at (a) surface (SFC), (b) lower troposphere (LT), (c) middle troposphere (MT), (d) upper troposphere , (e) lower stratosphere. Unit: °C. Other definitions can be found in Table 1.

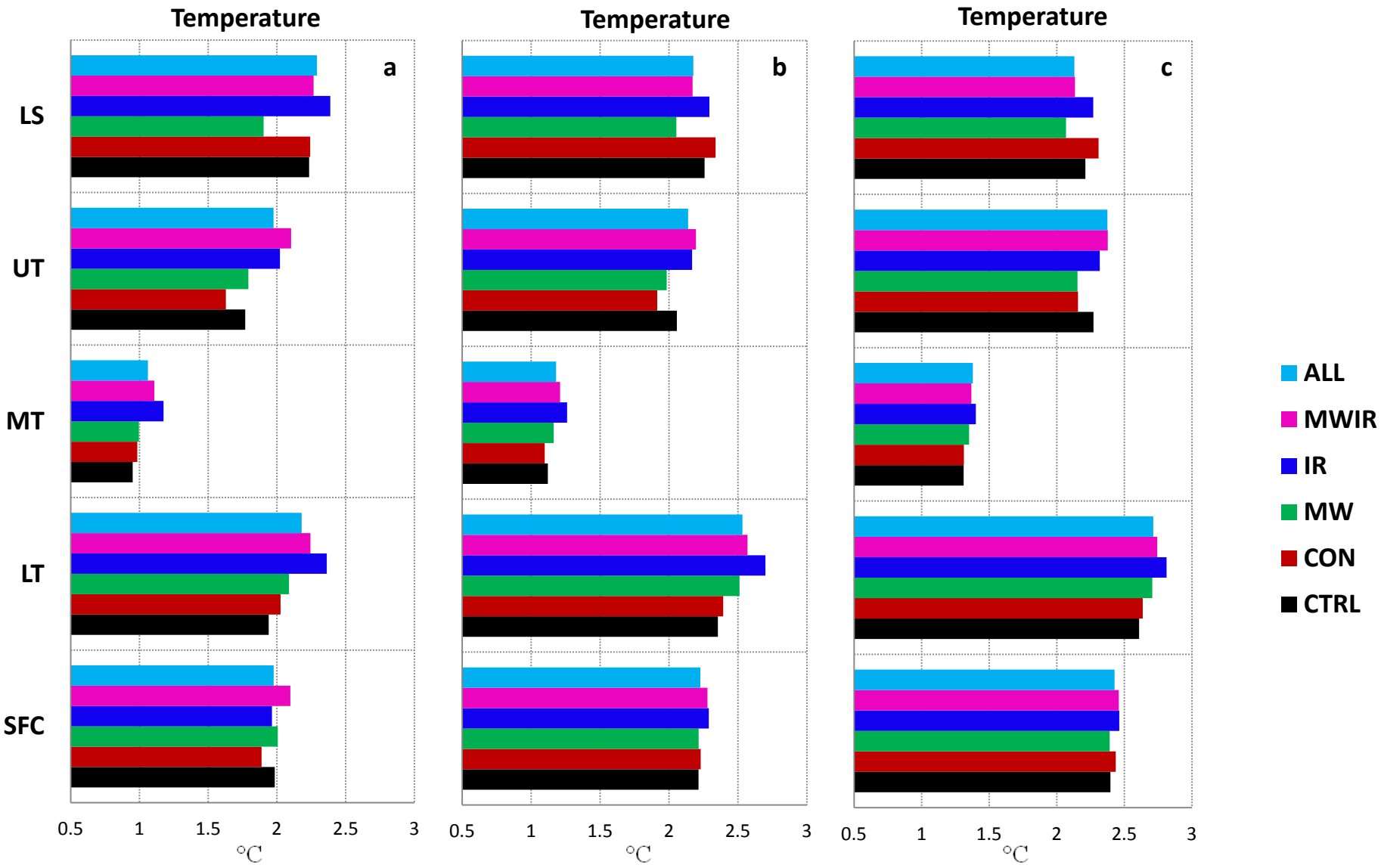

Fig. 7 The RMSE profile of the temperature forecasts at (a) 6-h , (b) 30-h, (c) 54-h forecasts. Unit: °C. Other definitions are the same of Fig. 4.

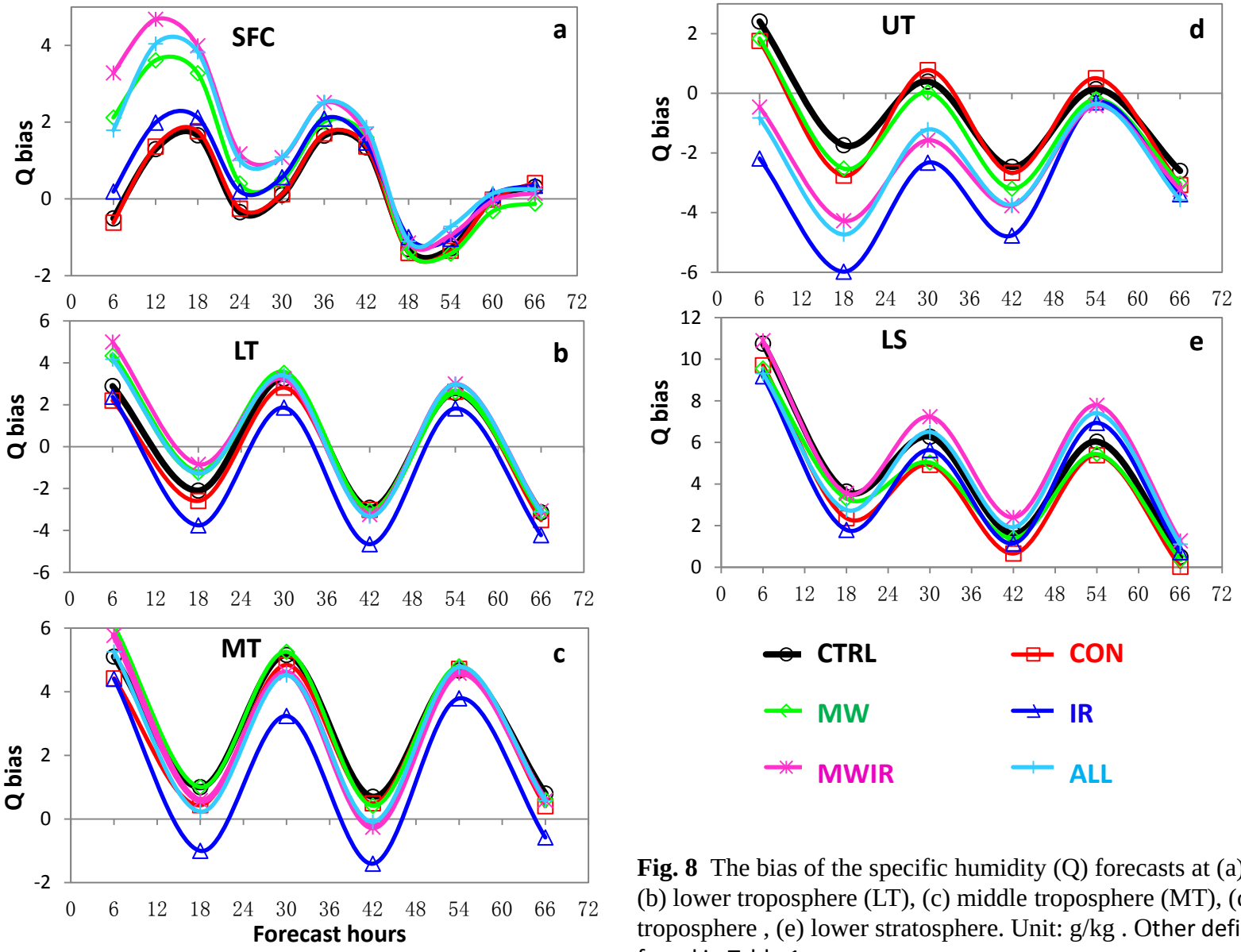

Fig. 8 The bias of the specific humidity (Q) forecasts at (a) surface (SFC), (b) lower troposphere (LT), (c) middle troposphere (MT), (d) upper troposphere , (e) lower stratosphere. Unit: g/kg . Other definitions can be found in Table 1.

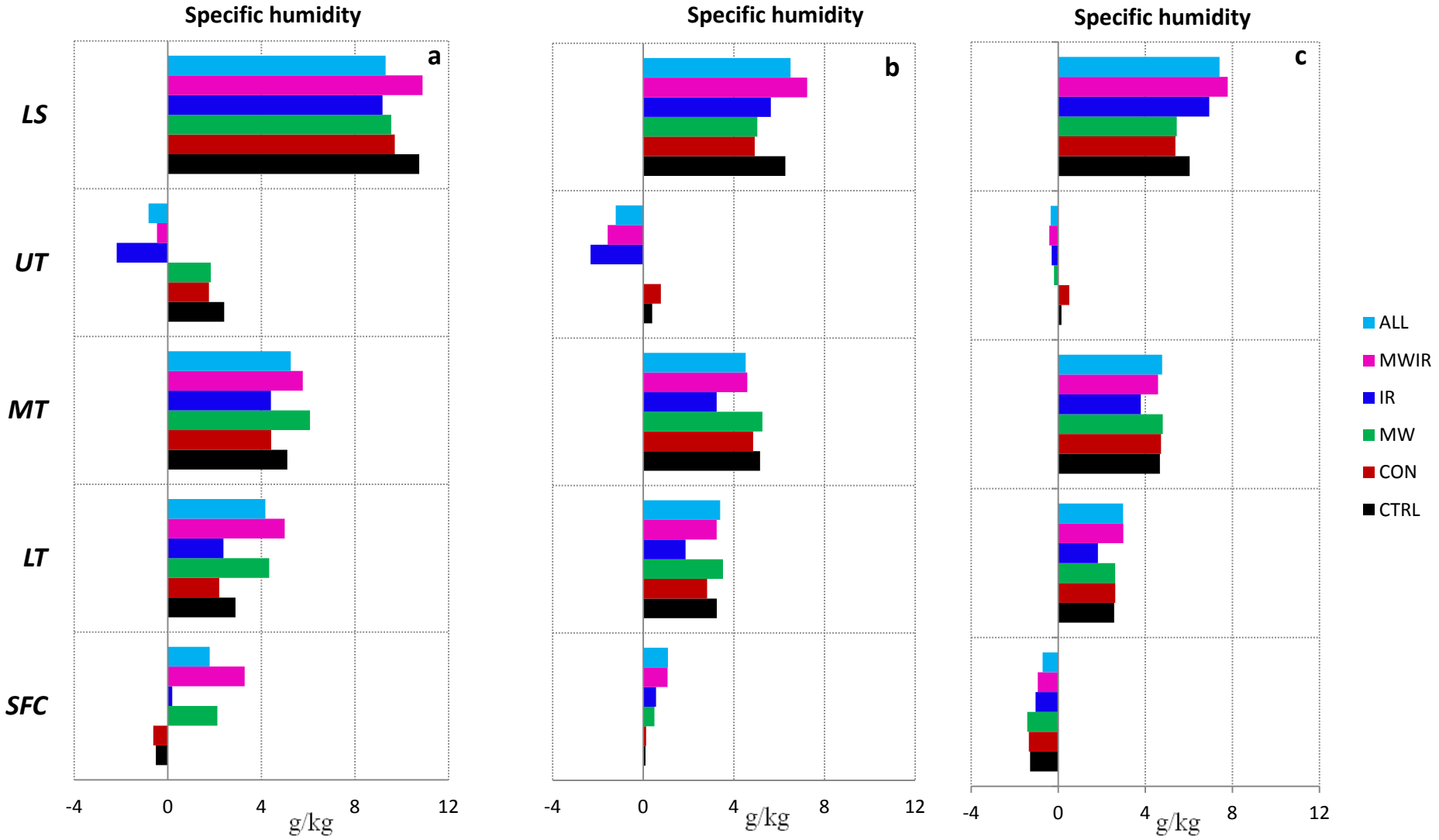

Fig. 9 Bias profile of the specific humidity forecasts at (a) 6-h , (b) 30-h, (c) 54-h forecasts. Unit: g/kg. Other definitions are the same of Fig. 4.

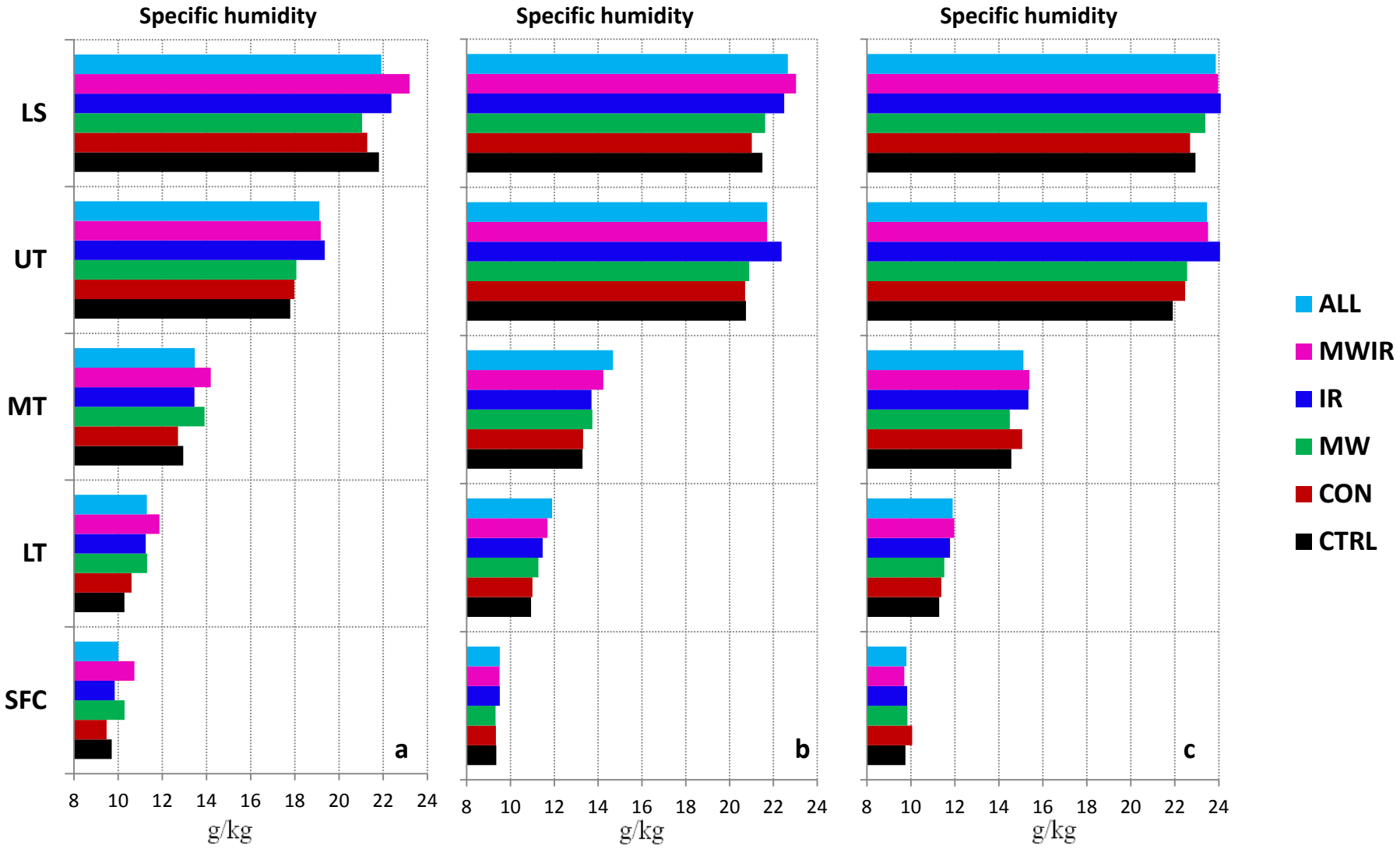

Fig. 10 The RMSE profile of the specific humidity forecasts at (a) 6-h , (b) 30-h, (c) 54-h forecasts. Unit: g/kg. Other definitions are the same of Fig. 4.